JOURNAL OF GEOPHYSICAL RESEARCH, VOL. 99, NO. C2, PAGES 3263–3272, FEBRUARY 15, 1994

Barotropic currents and vorticity in the central North Pacific Ocean during summer 1987 determined from long-range reciprocal acoustic transmissions

Brian D. Dushaw,[1] Peter F. Worcester, and Bruce D. Cornuelle

Scripps Institution of Oceanography, La Jolla, California

Bruce M. Howe

Applied Physics Laboratory, College of Ocean and Fishery Sciences, University of Washington, Seattle

Abstract. Large-scale depth-integrated currents and relative vorticity were measured in the central North Pacific Ocean during summer 1987 using long-range reciprocal acoustic transmissions between transceivers in a triangle approximately 1000 km on a side. Inverse techniques were used to estimate the depth-averaged (barotropic) current hourly at 4-day intervals from differential travel times. Tidal constituent amplitudes and phases found from the acoustically determined currents agree with those found from current meters and with the tidal models of Schwiderski (1980) and Cartwright et al. (1992), providing confirmation that the tomographically derived barotropic currents are correct within the expected uncertainties. The estimated low-frequency, large-scale currents are compared with depth-averaged currents determined by point measurements using current meters and bottom-mounted electrometers. Meridional and zonal currents are calculated using the topographic Sverdrup balance with the Fleet Numerical Oceanography Center wind field. The measured time derivative of the areally averaged relative vorticity is shown to be insignificant to the Sverdrup balance. Currents and vorticity calculated using the Sverdrup balance are an order of magnitude smaller than the observations. The magnitude and variability of the large-scale currents and vorticity determined from the Semtner and Chervin (1988) eddy-resolving model of ocean circulation are similar to the direct measurements.

1. Introduction

Three acoustic transceivers configured in a right triangle with sides 745, 995, and 1275 km long were deployed from May to September 1987 north of Hawaii between the subtropical and subarctic fronts (Figure 1). This experiment, called the 1987 Reciprocal Tomography Experiment, has been described by *Dushaw et al.* [1993a,b] (hereinafter referred to as DWCHa or b). Twelve hourly transmissions were made every fourth day. In this paper, range-averaged, depth-averaged currents are determined using linear inverse techniques on the differential travel times from reciprocal transmissions. (The depth-averaged current is also referred to here as the barotropic current.) Currents determined tomographically are inherently depth and range averaged. With the currents determined along three legs of a triangle, the barotropic gyre-scale relative vorticity can be determined [*Rossby,* 1975; *Longuet-Higgins,* 1982]. Preliminary determination of currents from these long-range transmissions has been reported by *Worcester et al.* [1990, 1991].

The experiment was located in the central North Pacific because the mesoscale activity is relatively low [*Emery,* 1983; *Shum et al.,* 1990], so there is little mesoscale noise in the measurements of gyre-scale averages. Three or four predominantly zonal fronts were present in the experiment area (DWCHa). A subsurface current meter mooring with vector measuring current meters (VMCMs) at 73, 173, 943, 2498, 5650, and 5722 m was deployed at 40.647°N, 163.025°W, between the northern transceiver moorings, from September 1986 through September 1987. This mooring will be referred to as the central mooring. The experiment was collocated with the Barotropic Electromagnetic and Pressure Experiment (BEMPEX) but only overlapped with it during May and June 1987 [*Chave et al.,* 1990, 1992; *Luther et al.,* 1987, 1990, 1991]. As part of BEMPEX, a number of bottom-mounted electrometers (EMs), magnetometers, and pressure sensors were deployed in the vicinity of the current meter mooring.

Section 2 describes the data used in the inversions. A tidal signal is found to account for about 90% of the observed differential travel time variance, providing an excellent test signal for the acoustically derived currents. At low frequency (<1 cpd), all multipath travel times show nearly identical behavior. In section 3 the inversion of the acoustic data for the current is described. The inversions of the acoustic travel times for the current are made using time-dependent ray paths and the sound speed field determined from the sum travel times (DWCHb). Section 4 compares the acoustically determined barotropic currents with those determined from the bottom-mounted electrometers in BEMPEX, the central mooring current meters, and the *Schwiderski* [1980] and *Cartwright et al.* [1992] (hereinafter referred to as CRS) tidal models.

Although the record length of the present experiment is short (about 100 days), the measured currents provide a good test of

[1]Now at the Applied Physics Laboratory, University of Washington, Seattle.

Paper number 93JC03335.
0148-0227/94/93JC–03335$05.00

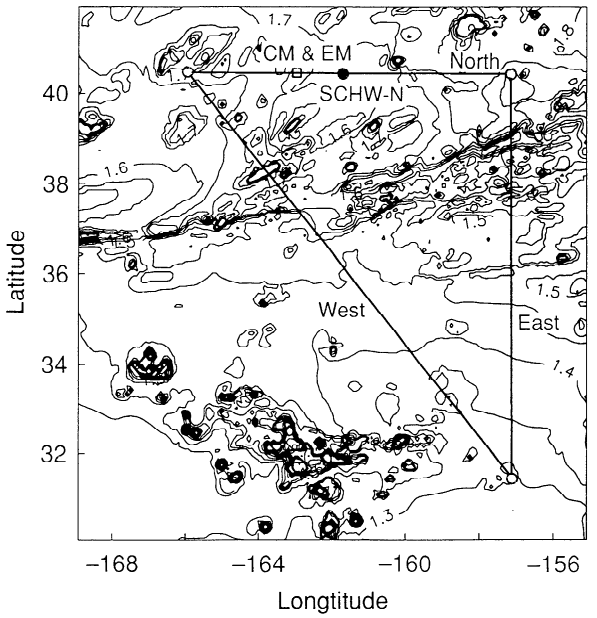

Figure 1. Geometry of the 1987 gyre-scale reciprocal acoustic transmission experiment superimposed on contours of f/H. The acoustic transceivers are located at the circles. CM & EM (square) is the location of a current meter mooring and electromagetic field sensor. SCHW-N (solid circle) is the location for which results of the Schwiderski numerical tide model are given. North, east, and west are the names given to the legs of the triangle. The triangle is located north of Hawaii between the subtropical and subarctic fronts. The Musicians Seamounts are evident in the bottom left-hand corner. The f/H contour intervals are 0.05×10^{-8} m^{-1} s^{-1}.

the topographic Sverdrup balance [*Cummins,* 1991; *Koblinsky,* 1990]. With currents that are averaged over 1000-km length scales, both mesoscale variability (almost negligible in this region) and small-scale topographic effects are reduced. Since the barotropic currents are determined to an accuracy of a few millimeters per second and since at 1000-km scales the beta effect, which governs the Sverdrup response, is important for time periods greater than a half day, the local Sverdrup equilibrium should be apparent. In section 5 the measured currents are compared with the Sverdrup balance currents calculated using Fleet Numerical Oceanography Center (FNOC) wind data and ETOPO-5 (Earth topography, 5 minutes) bathymetry data. Currents and vorticity calculated using the Sverdrup balance are an order of magnitude smaller than the observations, which suggests the origin of the observed variability is nonlocal.

In section 6 the order of magnitude of the acoustically determined currents and vorticity are compared with results from the *Semtner and Chervin* [1988] eddy-resolving global ocean circulation model. Section 7 discusses our results and gives our conclusions.

2. Travel Times

Acoustic propagation varies due to perturbation of the sound speed and current fields by gyre and mesoscale processes, internal waves, inertial currents, tides, wind forcing, and other oceanographic phenomena. The one-way travel time, T_i, for each ray path, Γ_i, is given by

$$T_i(t) = \int_{\Gamma_i} \frac{ds}{c(\mathbf{x}, t) + \mathbf{u}(\mathbf{x}, t) \cdot \boldsymbol{\tau}} \qquad (1)$$

where $c(\mathbf{x}, t)$ is the sound speed field, $\mathbf{u}(\mathbf{x}, t) \cdot \boldsymbol{\tau}$ is the component of three-dimensional current velocity in the direction of the ray path, ds is an increment of arc length, and t is geophysical time. In this experiment, only deep-turning, surface-reflected rays and an axial ray (the ray that remains near the sound channel axis) are available (Figure 2). The axial ray corresponds to the slowest acoustic pulse travel time. The measured travel times are corrected for clock error and mooring motion (DWCHa).

The difference in the travel times of oppositely traveling signals depends, in the linear approximation, only on the current component along the line between the transceivers, as will be shown in detail in section 3. The raw, detided, and high-frequency differential travel times for the first few days of the time series on the north leg are shown in Figure 3. Data outside of about ±40 ms are considered outliers and have been removed from the time series. The variance of the high-frequency time series is primarily due to internal and inertial wave-induced fluctuations [*Flatté et al.,* 1979]. One goal of this section is to estimate the uncertainty of the differential travel times from the high-frequency differential travel time series. To calculate the high-frequency variances, the tides are removed from the raw differential travel times using a least squares fit of eight tidal frequencies to the entire time series for each ray path separately. The tidal signal accounts for about 90% of the total variance. The detided differential travel times are then high-pass filtered (>1 cpd) to obtain the high-frequency differential travel times.

Figure 4 shows the low-frequency differential travel times for all three legs. The travel times on the west leg suffer from a low signal-to-noise ratio because of the long range. Current shear causes the differential travel times for the north leg axial and deep-turning ray data to be significantly different. These low-

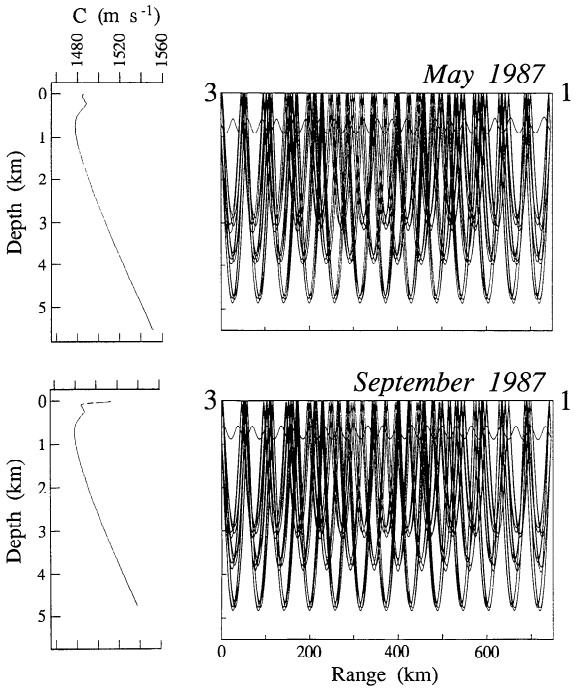

Figure 2. Sound speed profiles and ray paths for the northern leg of the triangle. Only resolved ray paths are shown, and the path for the slowest acoustic energy is represented as the axial ray near 800-m depth. The change in sound speed profile from May to September is mostly due to the formation of the summer thermocline. In May, all of the ray paths are surface reflected, but in September some of the paths have turning points at the bottom of the summer thermocline. Modified from *Worcester et al.* [1991].

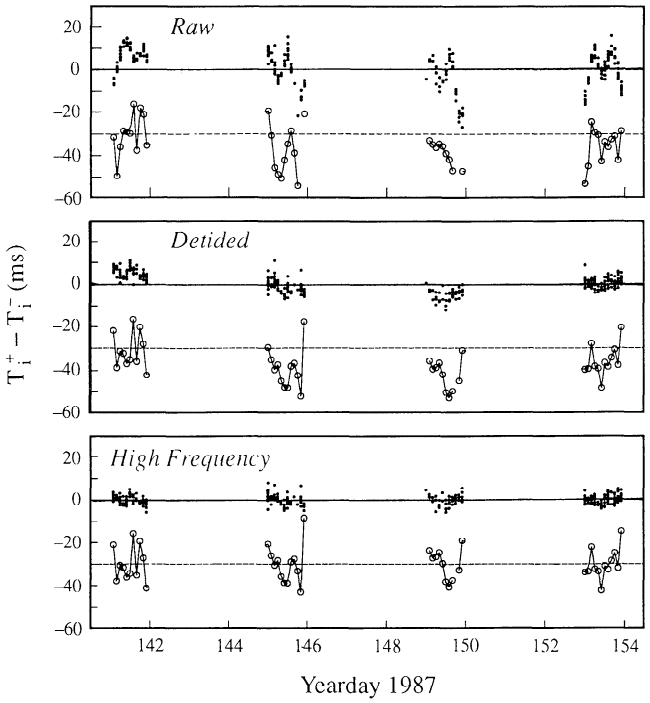

Figure 3. The raw, detided, and high-frequency (>1 cpd) differential travel times for the first few days of the time series on the north leg. Small solid circles are data from the deep-turning rays, while open circles are data from the axial ray, which have been offset by 30 ms.

frequency time series are not actually used for the inversions presented in this paper. Rather, the tides and low-frequency currents are determined in the next section by inverting the data from each transmission for current before extracting the tidal signal from the time series of depth-averaged current. After removing the tidal signal, daily-average currents are computed. This procedure provides a better estimate of the barotropic tides than can be obtained by estimating the tidal signal for each ray path separately (as was done by *Worcester et al.* [1991]).

While large shear can cause nonreciprocal ray paths by refracting oppositely traveling rays differently, reciprocity, required for the linearization of (1), can be tested by examining the high-frequency travel time variances. The high-frequency (>0.5 cpd) travel time variability is largely due to internal wave displacement of isotachs. If the oppositely traveling signals follow the same ray path, sound speed fluctuations induced by internal waves cancel in forming the differential travel times, except for changes in the internal wave field that occur during the approximately 10-min-long travel times. The high-frequency variances of the east leg one-way travel times are 20–56 ms^2, while one-half the variances of the differential travel times are 7–21 ms^2 (Table 1), for example. The sum and one-way travel time variances in Table 1 also include a contribution due to isotach displacements by the baroclinic tide. If the high-frequency variabilities of reciprocal transmissions were uncorrelated, the variance of the differential travel times would be twice that of the one-way travel times. The reduction in high-frequency variance for the differential travel times demonstrates that the reciprocal transmissions are sampling a similar internal wave field. This is a sufficient but not necessary condition for reciprocity, since we are generally interested in scales much larger than internal wave correlation scales. The degree of reciprocity depends on the transmission range. At 300-km range, *Howe et al.* [1987] measured high-frequency (>0.5 cpd) variances of one-way and differential travel times to be 10.6 ms^2 and 0.4 ms^2, respectively, showing greater reciprocity than observed at the much longer ranges in this experiment.

The uncertainty of the one-way travel times is dominated by uncertainty in mooring motion correction and by fluctuations induced by internal waves. Pulse compression techniques allow the raw travel times to be measured to 1-ms precision. The mooring motion correction cancels in forming the differential travel times, although the mooring motion correction uncertainty is small (roughly 2 ms rms) in any event [*Munk and Wunsch,* 1982]. The uncertainty in the clock correction contributes less than a millisecond to the uncertainty in the differential travel times [*Worcester et al.,* 1985]. To good approximation the total uncertainties in the one-way and differential travel times are given by their respective high-frequency variances.

3. Inversions and Vorticity

Howe et al. [1987] describe the method used to invert the differential travel times for current. Equation (1) can be linearized by expanding it in the small parameter $\mathbf{u}(\mathbf{x}, t)\cdot\tau/c_0(\mathbf{x}, t)$, where $c_0(\mathbf{x}, t)$ is a reference time-dependent sound speed field. The difference of the travel times of oppositely traveling pulses gives

$$T_i^+(t) - T_i^-(t) \approx -2\int_{\Gamma_i} \frac{\mathbf{u}(\mathbf{x}, t)\cdot\tau}{c_0(\mathbf{x}, t)^2}\, ds \qquad (2)$$

The differential travel time depends linearly on the current field. The solution by DWCHb for the time evolution of sound speed is used as the reference $c_0(\mathbf{x}, t)$, to properly account for the ray path changes over the course of the experiment. (The reference sound speed field has been determined to within 1 m/s, compared

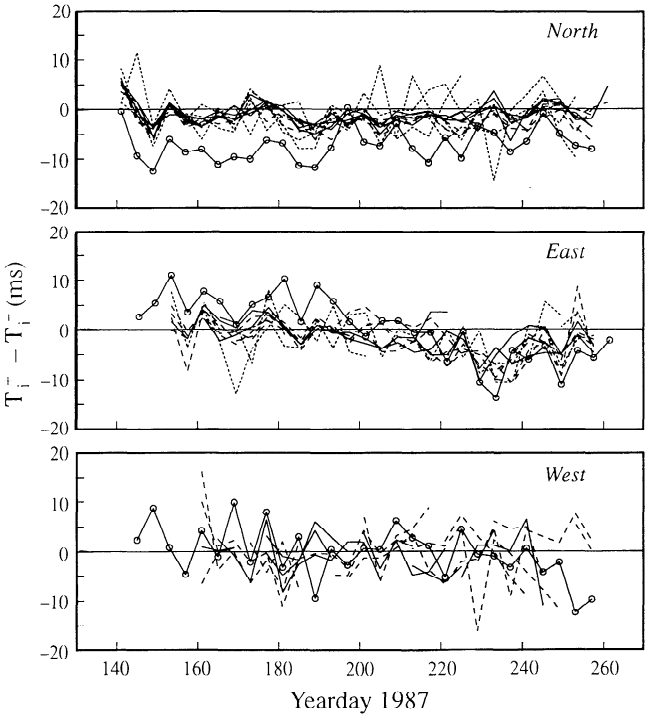

Figure 4. The low-frequency (<1 cpd) differential travel times for all three legs. The ray groups (see Figure 2) are distinguished by solid, dashed, and dotted curves. Current shear is evident in the dispersal of the axial ray travel times (circles) from the deep-turning ray travel times.

Table 1. Detided, High-Frequency (>1 cpd) Travel Time Variances

		$\langle(T^+)^2\rangle$ ms^2	$\langle(T^-)^2\rangle$ ms^2	$\frac{1}{2}\langle(T^+ + T^-)^2\rangle$ ms^2	$\frac{1}{2}\langle(T^+ - T^-)^2\rangle$ ms^2
North	rays 1–4	10	12	17	3
	rays 5–8	17	19	27	6
	rays 9–12	41	50	70	15
	axial	153	129	198	41
East	rays 2,4	20	19	26	7
	rays 5–8	29	25	35	13
	rays 9–12	56	31	63	21
	axial	193	177	246	52
West	rays 1,2,4	14	20	23	7
	rays 5,6,7	44	62	63	10
	axial	227	249	338	77

The variances of the sum and difference travel times have been divided by 2 for comparison with the one-way variances.

to a 1500 m/s nominal sound speed value, hence its error is insignificant to the solution for current.) The solution for current is expressed as a linear combination of functions of range and depth whose amplitudes are functions of time:

$$\mathbf{u}(\mathbf{x}, t) = \sum_{j=1}^{N} A_j(t) F_j(\mathbf{x}) \hat{\mathbf{u}} \tag{3}$$

where $A_j(t)$ are the amplitudes of the N two-dimensional basis functions, $F_j(\mathbf{x})$, and $\hat{\mathbf{u}}$ is a unit vector from the source to the receiver. (The current components perpendicular to the transmission path and in the vertical have a negligible effect and are neglected hereinafter.) Inserting (3) in (2) gives

$$T_i^+ - T_i^- = -2 \int_{\Gamma_i} \frac{\sum_{j=1}^{N} A_j(t) F_j(\mathbf{x}) \hat{\mathbf{u}} \cdot \boldsymbol{\tau}}{c_0(\mathbf{x}, t)^2} ds \tag{4}$$

Dropping the time dependence, define

$$T_i^+ - T_i^- = \sum_{j=1}^{N} G_{ij} A_j \tag{5}$$

Here

$$G_{ij} = -2 \int_{\Gamma_i} \frac{F_j(\mathbf{x}) \cos\theta}{c_0(\mathbf{x}, t)^2} ds \tag{6}$$

where $\cos\theta = \hat{\mathbf{u}} \cdot \boldsymbol{\tau}$ is the ray angle relative to the horizontal. Stochastic inverse methods [*Aki and Richards*, 1980; *Howe et al.*, 1987] are used to solve (5) for the A_j. The $F_j(\mathbf{x})$ consist of a mixed layer function, a depth-independent mode, and a set of orthogonal functions (see DWCHb) in the vertical and truncated Fourier series in the horizontal. Figure 5 shows the vertical functions, a priori variance, and covariances assumed for the stochastic inverse. The horizontal a priori covariance is the Fourier transform of the assumed spectrum (weighting) of wavenumbers. The vertical a priori covariance is similar to the horizontal covariance, with the role of the sines and cosines replaced by the vertical functions.

The structure of the ray paths determines the amount of spatial information that can be extracted. The deep-turning rays sample almost the entire water column. The axial ray gives information about the sound channel axis. The absence of rays

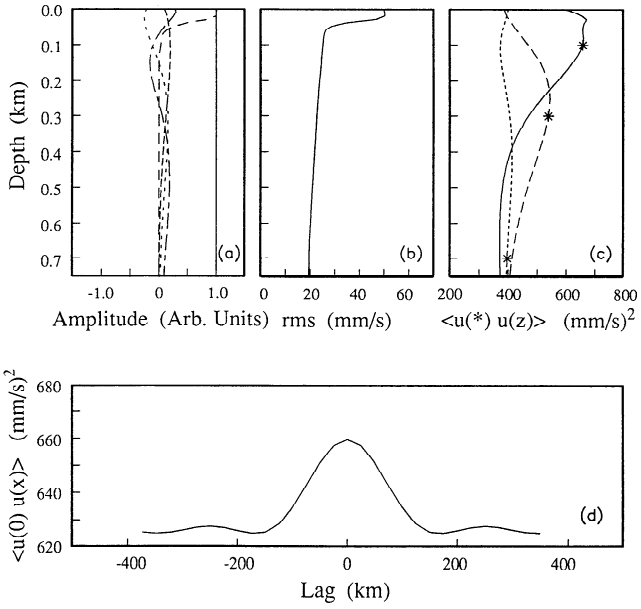

Figure 5. (a) Vertical functions, (b) depth-dependent a priori rms current, (c) vertical covariance, and (d) horizontal covariance used in the stochastic inverse. The first vertical function (solid) is the barotropic mode. The second vertical function (medium dashed) is a mixed layer function (see DWCHb) and is evident in the rms depth-dependent current variability. The horizontal (vertical) covariance does not fall to zero because the range-independent (depth independent) mode accounts for most of the variance.

with upper turning points at intermediate depths causes the baroclinic structure of the current to be poorly resolved in this experiment. Thus compared with the true current profile, the inverse solution may be too fast at one depth and correspondingly too slow at another depth. While the uncertainty in the inverse solution at any particular depth may be large, the uncertainty of the depth integral of the inverse solution is nonetheless small, since the inverse uncertainty is correlated with depth.

Thus only depth-averaged solutions are given in this paper (Appendix).

The areally averaged relative vorticity can be found, using Stokes' theorem, by integrating the acoustically determined currents cyclonically around the experiment triangle and dividing by the enclosed area. This is calculated as

$$\omega = -(1/A)\times(745\times10^3\, U_N - 996\times10^3\, U_E + 1275\times10^3\, U_W) \quad (7)$$

where ω is the vorticity, A is the area enclosed by the triangle, U_N is the eastward current from the north leg, U_E is the northward current from the east leg, U_W is the northwestward current from the west leg, and the constants are the ranges of the respective legs in meters (Figure 1). It is not possible to use the difference in anticlockwise and clockwise sing-around travel times to calculate the vorticity directly from the travel times [*Munk and Wunsch,* 1982], because of the different ray path sampling characteristics on each leg of the triangle.

4. Comparison Between Range-Average (Determined Acoustically) and Point Measurements of Barotropic Currents

This section compares the acoustically determined tidal and low-frequency currents with current meter and EM measurements. The unfiltered differential travel times are inverted to obtain current estimates bihourly every fourth day. The currents are detided before calculating the low-frequency (daily average) component.

The K_2, S_2, M_2, N_2, K_1, P_1, O_1, and Q_1 tides are estimated using weighted least squares, taking into account the uncertainty in the current estimates and a priori magnitudes of the tidal amplitudes (Appendix). (The elevation amplitude of the lunar fortnightly tidal constituent (Mf) [*Schwiderski,* 1982], when compared with the elevation and current amplitudes of the major tidal constituents, shows that the Mf tidal current is less than 0.5 mm/s, so it is neglected.) The current uncertainty includes the nontidal high-frequency variability. The tidal harmonic constants are not sensitive to the assumptions in the analysis. Previous results from an unweighted least squares fit of the tidal constituents to the differential travel times do not differ significantly from these results [*Worcester et al.,* 1991; *Luther et al.,* 1991]. The weighted least squares technique also gives the uncertainty in the constituent amplitudes and phases. (The uncertainties reported by *Worcester et al.* [1991] and *Luther et al.* [1991] were preliminary and resulted from a simple root-mean-square of separate tidal analyses on the travel times from each ray.) The tidal estimates test the accuracy of the acoustically determined currents. The tidal currents are reasonably well known, barotropic, and have length scales much larger than the acoustic path lengths. The results for the zonal tides agree with barotropic tides determined from the central current meter mooring [*Luther et al.,* 1991] and differ slightly from the results of the *Schwiderski* [1980] and CRS numerical models (Table 2). Tidal results from the other two legs also compare favorably with the Schwiderski and CRS tidal models (not shown). The amplitudes of Table 2 include the lunar node factor to account for the revolution, with 18.6-year period, of the Moon's node [*Schureman,* 1958]. Baroclinic tidal currents negligibly affect the differential travel times due to the vertical averaging inherent in the measurements [*Munk et al.,* 1981].

The uncertainty estimates in Table 2 show that the large-scale, barotropic tidal currents are about as accurately determined from the acoustic transmissions as from the year-long current meter data. (The uncertainties for the current meter results were estimated by *Luther et al.* [1991] following Appendix B of *Munk and Cartwright* [1966].) Six current meters were used by *Luther et al.* [1991] to estimate the barotropic current by projecting the data onto the gravest structure function appropriate for horizontal currents at low frequencies (with respect to the average buoyancy frequency profile derived from several conductivity-temperature-depth (CTD) casts taken near the BEMPEX mooring). A lack of coherence between adjacent current meters was frequently observed, and the deeper current meters stalled in weak currents (the rated stall speed was about 1 cm/s). *Luther et al.* [1991] found that the zonal barotropic currents determined from the current meters required scale factor correction of 1.48 (included here) in order for them to agree with the low-frequency barotropic currents obtained from the electrometer data. The EM measurements cannot accurately determine the tides because of ionospheric noise. A spectrum of the barotropic current determined from the current meters shows a large inertial peak, indicating that internal and inertial waves were aliased into the barotropic current. While the barotropic tides account for about 90% of the observed variance in the acoustically determined currents, the tides account for only 25% of the variance of the current-meter-derived barotropic current, because of internal and inertial wave noise and stalling.

Figure 6 shows the low-frequency (daily averaged) currents for each leg and the areally averaged relative vorticity. The low-frequency current and uncertainty were calculated using weighted least squares to daily average the detided current time series. The uncertainty derived from the inverse of travel times

Table 2. Amplitude and Greenwich Epoch of the Eastward Barotropic Tidal Currents for the North Leg

Tidal Constituent	Amplitude, cm/s				Greenwich Phase, °G			
	Acoustic Tomography	Current Meter Mooring	Schwiderski Model	CRS[a] Model	Acoustic Tomography	Current Meter Mooring	Schwiderski Model	CRS[a] Model
K_2	0.12±0.04	0.10±0.04	—	0.14	268±13	280±21	—	279
S_2	0.53±0.04	0.53±0.05	0.66	0.63	272± 4	280± 6	270	276
M_2	1.31±0.03	1.32±0.05	1.28	1.42	223± 1	218± 2	222	218
N_2	0.14±0.03	0.15±0.05	0.16	0.15	191±13	216±17	184	201
K_1	0.75±0.04	0.74±0.03	0.45	0.53	128± 2	135± 3	127	100
P_1	0.18±0.04	0.27±0.02	—	0.10	132±11	141± 4	—	129
O_1	0.43±0.03	0.46±0.03	0.33	0.38	101± 4	122± 4	99	104
Q_1	0.10±0.03	0.07±0.02	—	0.05	64±16	110±14	—	125

[a]The CRS model is the Cartwright, Ray, and Sanchez model.

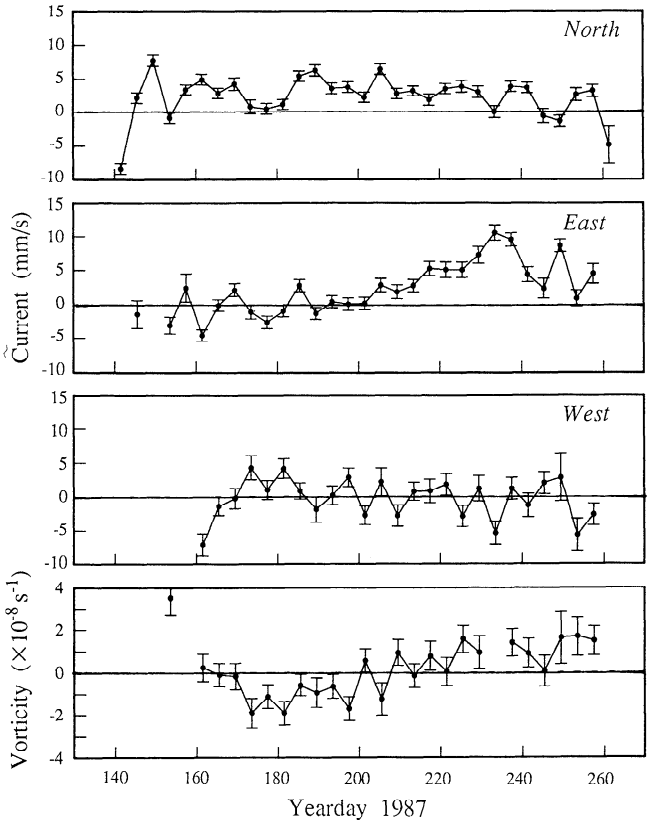

Figure 6. The low-frequency (daily averaged) currents for each leg and the areally averaged relative vorticity. The vorticity is calculated by integrating the currents around the experiment triangle. The calculation of vorticity cancels much of the variability in the currents.

from each transmission was used as the weighting in this calculation, so that the different uncertainties from each inversion are properly taken into account. The uncertainty for vorticity is found by combining the uncertainties in U_N, U_E, and U_W in quadrature, weighted according to (7).

A significant fraction of the variability present in the time series of current cancels in the calculation of vorticity. This can be shown by calculating the "vorticity" using an incorrect sign for the east leg. The variance of the incorrectly calculated "vorticity" is 3 times that of the observed vorticity. The partial cancelation of the variability is consistent with the observation that variability at periods longer than a few days corresponds to megameter wavelengths in this region [*Chave et al.*, 1992].

The acoustically derived, low-frequency zonal current is compared with the current meter and EM zonal currents on the north leg (Figure 7). The current meter data were processed to give barotropic currents, which were low-pass filtered with a one-day running mean, then daily averaged, for direct comparison with the acoustically determined currents. This procedure eliminated much of the aliased inertial energy. Barotropic currents measured by the horizontal electric field instruments in BEMPEX were filtered in the same manner as the current meter data. *Luther et al.* [1991] found that the mean (time averaged) barotropic currents from nearby current meter and electrometer data disagreed significantly. They speculated that the discrepancies were due to the horizontal averaging inherent in the electromagnetic measurements and to the effect of planetary vorticity (f/H) variability on the barotropic flow. To compare the electromagnetic, current meter, and acoustic currents, the time averages are therefore removed. The mean and rms of the current meter and acoustic time series from year days 140 to 260 are +11.2 ± 5.4 mm/s and +2.0 ± 2.9 mm/s, respectively. The acoustic, current meter, and electrometer data all show a strong westward barotropic flow of 10–15 mm/s near year day 145 on the north leg. Subsequently, the acoustically derived currents show much less variability than the current meter data. This is expected, since the current meter and electric field measurements are made at a point, while the range-average acoustic measurements strongly suppress small-scale and mesoscale variability. The extent to which agreement is observed indicates that the barotropic component of flow is large scale. Unfortunately, the time series are too short to compute meaningful correlation coefficients.

5. Sverdrup Balance

The topographic Sverdrup balance [*Sverdrup*, 1947; *Willebrand et al.*, 1980] can be used to make an estimate of the expected wind-driven barotropic current and relative vorticity on 1000-km scales. A number of recent papers [*Müller and Frankignoul*, 1981; *Niiler and Koblinsky*, 1985; *Koblinsky et al.*, 1989; *Koblinsky*, 1990; *Cummins*, 1991; *Luther et al.*, 1990; *Chave et al.*, 1992] have discussed the local wind-driven flow (flow along contours of $\nabla(f/H)$, where f is the inertial frequency and $H(x,y)$ is the topography) and nonlocal wind-driven flow (flow along contours of f/H). *Müller and Frankignoul* [1981], *Niiler and Koblinsky* [1985], *Koblinsky et al.* [1989], *Luther et al.* [1990], and *Chave et al.* [1992] have discussed wind forcing as the origin of mid-ocean mesoscale variability. *Koblinsky et al.* [1989] found a seasonal modulation of ocean kinetic energy beneath the main thermocline which corresponded with the seasonal modulation of the local wind stress curl field. *Luther et al.* [1990] and *Chave et al.* [1992] described significant coherences of currents measured in BEMPEX with nonlocal atmospheric forcing. Observation of locally driven Sverdrup transport has been observed in only a few cases [*Niiler and Koblinsky*, 1985; *Koblinsky et al.*, 1989; *Brink*, 1989; *Samelson*, 1990; *Luther et al.*, 1990; *Chave et al.*, 1992]. Through numerical experiments

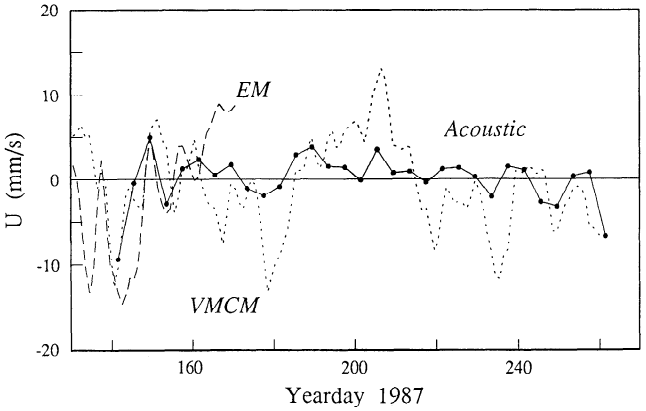

Figure 7. Comparison of the acoustic (solid), current meter (VMCM, dotted), and electromagnetic (EM, dashed) zonal currents. The acoustically determined currents are for the north leg. The current meter and electromagnetic data have been smoothed with a 1-day running mean filter, before daily averaging. The means have been removed from each time series (see text).

with a stochastically forced, barotropic, quasigeostrophic model of the subpolar North Pacific, *Cummins* [1991] found the topographic Sverdrup balance to be evident for periods longer than about 40 days when averages over 4° × 4° regions were taken. At shorter periods a surface-trapped evanescent response is expected [*Willebrand et al.*, 1980]. *Koblinsky et al.* [1989] found that the Sverdrup balance was evident at only a few of the 31 locations where current meter data were examined, for currents with periods from 10 to 100 days and when the topographic variability was averaged over a 175-km length scale. *Koblinsky et al.* [1989] argued that the Sverdrup balance is difficult to observe because the topography in the North Pacific generally enhances the beta effect and thus diminishes the observable Sverdrup response.

In the present experiment, currents are averaged over 1000-km scales; both mesoscale variability and small-scale topographic effects are therefore reduced. The measurements determine the depth-integrated, range-averaged current to within a few millimeters per second. These qualities of the measurements make them good for testing the validity of the local Sverdrup balance, but the estimated Sverdrup currents are an order of magnitude less than the observed currents.

Cummins [1991] provides a brief summary of the equations relevant to the topographic Sverdrup balance. The linear vorticity equation for the forced quasi-geostrophic flow of a homogeneous fluid over topography is

$$(\nabla^2 - \frac{f^2}{gH})\psi_t + H J(\psi, f/H) = \hat{\mathbf{k}} \cdot \nabla \times \frac{\tau}{H\rho} \tag{8}$$

where g is gravitational acceleration, ψ is a stream function, J is the Jacobian, ρ is density, $\hat{\mathbf{k}}$ is an upward unit vector, and τ is wind stress. A characteristic timescale [*Willebrand et al.*, 1980; *Koblinsky*, 1990] of the above equation is

$$T = L\beta^{-1}(L^{-2} + f^2/gH) \tag{9}$$

This timescale measures the importance of the beta effect in the oceanic response to forcing; the response at periods much larger than T is governed by the Sverdrup balance. For $L = 1000$ km, T is about 0.5 day. For slowly varying currents (so the time derivative terms can be omitted), (8) reduces to the topographic Sverdrup balance,

$$H\mathbf{u} \cdot \nabla(f/H) = \hat{\mathbf{k}} \cdot \nabla \times \frac{\tau}{H\rho} \tag{10}$$

This approximation omits the time derivative of the relative vorticity, a term which we have estimated from the vorticity time series. Figure 1 shows the contours of planetary vorticity, or f/H, in the region of the experiment. The topographic Sverdrup gain function,

$$G = \frac{\beta/H}{|\nabla(f/H)|} \tag{11}$$

which is the ratio of the response to the wind forcing in the flat-bottom case to that in the topographic case, is generally about 0.2–0.6 in the experiment area (Figure 8, which has been smoothed for illustration purposes). The average gain along the east leg is about 0.4.

The U.S. Navy Fleet Numerical Oceanography Center (FNOC) wind field was used to estimate wind forcing. Many recent investigations comparing measured currents with atmospheric forcing have used the FNOC wind field to estimate the wind stress and its curl [*Niiler and Koblinsky*, 1985; *Brink*, 1989; *Koblinsky et al.*, 1989; *Luther et al.*, 1990; *Samelson*, 1990; *Chave et al.*, 1992]. *Chave et al.* [1991] discuss the work by others comparing the FNOC product with direct measurements. The comparison is generally favorable, though the highly smoothed nature of the FNOC wind fields presents possible problems in interpreting the derived wind stress curl, especially at short length scales [see *Chave et al.*, 1991]. The FNOC product smooths mesoscale atmospheric disturbances, for example. *Pazan et al.* [1982] have shown that in regions where actual observations available for incorporation into the FNOC product are limited, the agreement of the FNOC winds with measured winds is poor. However, given the generally favorable comparison with direct measurements and the interesting results obtained by the above mentioned authors, it appears that the FNOC wind product is useful.

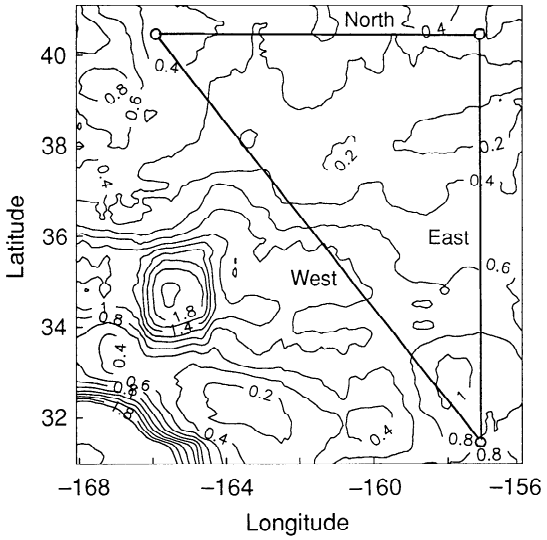

Figure 8. The topographic Sverdrup gain $(\beta/H)/|\nabla(f/H)|$ in the experiment region calculated using ETOPO-5 bathymetric data. The gain has been smoothed using a 170×140 km^2 running area average.

The bulk formulae of *Large and Pond* [1981] were used to compute the wind stress. Neutral stability was assumed to reduce the 19.5-m height FNOC winds to 10-m height, as required for the bulk formulae. The areally averaged wind stress curl was computed using Stokes' theorem,

$$\overline{\hat{\mathbf{k}} \cdot \nabla \times \tau} = (1/A) \oint \tau \cdot d\mathbf{s} \tag{12}$$

on the data from adjacent grid points. (The procedure to calculate wind stress curl from the FNOC winds is described in detail by *Koblinsky et al.* [1989].) We write $\nabla(f/H) = \hat{\mathbf{n}}|\nabla(f/H)|$, where $\hat{\mathbf{n}} = (n_1, n_2)$ is a unit vector in the direction of $\nabla(f/H)$. Thus from (10) the topographic Sverdrup current is (approximating ρH as constant in the curl)

$$(u, v) = (n_1, n_2) \frac{\hat{\mathbf{k}} \cdot \nabla \times \tau}{H^2 \rho |\nabla(f/H)|} \tag{13}$$

The current (u, v) is calculated at each grid point of the ETOPO-5 bathymetric data. The Sverdrup currents at each grid point are then averaged over an area 1° wide (in latitude or longitude) spanning the acoustic path. Doubling the width of the averaging region has negligible effect on this calculation. The "Sverdrup" vorticity is calculated by integrating the Sverdrup current around the triangle. The computed currents are an order of magnitude less than the measured currents (Table 3).

Table 3. Comparison of the Root-Mean-Square of the Sverdrup Balance, Semtner-Chervin Model, and Direct Measurements

	Sverdrup	Semtner-Chervin	Measured
North, mm/s	0.04	1.3	2.9
East, mm/s	0.45	0.7	3.3
West, mm/s	0.39	0.9	2.4
Vorticity ($\times 10^{-8}$ s^{-1})	0.06	0.4	1.1

Although part of this discrepancy may be due to the smoothed nature of the FNOC wind field, any mesoscale atmospheric forcing intense enough to account for the observed zonal current would cause inordinately large meridional current (Table 3 roughly compares the zonal (north leg) and meridional (east leg) responses to wind forcing). Further, significant local mesoscale atmospheric forcing of oceanic mesoscale variability would result in currents uncorrelated between each leg or, equivalently, significantly larger relative vorticity than that observed. We conclude that the Sverdrup transport does not account for the observed variability and that the currents are dominated by nonlocal forcing, which is consistent with the conclusions of *Chave et al.* [1992]. Unfortunately, the time series is too short to test the Sverdrup balance at long timescales (O(50–100 days)) and does not include strong wintertime forcing, when the Sverdrup balance may be more observable.

Ekman transport is not important to this comparison. The depth average of the Ekman transport is an order of magnitude smaller than the Sverdrup transport, and the current variability is evident in the travel times of the 500- to 900-m-deep axial ray (Figure 4), which is unaffected by surface currents.

Using the measured areal average vorticity, we can examine the importance of $\nabla^2\psi_t \approx \omega_t$ in (8). (For $L \approx$ 1000-km length scales, the second term is negligible: L^{-2} is ten times as big as f^2/gH.) At short timescales, ω_t is expected to balance the wind forcing. By area averaging the wind forcing in (8), the expected ω_t at short timescales (<4 days) is found to be of the order of 10^{-13} s^{-2}. The order of magnitude of the wind-forced change in areally averaged vorticity over a 4-day period is then about 3×10^{-8} s^{-1}. This order of magnitude is comparable to both the observed change and the uncertainty, so this comparison is inconclusive. At the longer Sverdrup-balance timescales the measured relative vorticity increases by about 2×10^{-8} s^{-1} in about a hundred days. This roughly corresponds to $\omega_t = 10^{-15}$ s^{-2}, which is an order of magnitude smaller than $H\mathbf{u}\cdot\nabla(f/H)$, for u = 1 mm/s. For this one realization, ω_t is verified as a small term in (8).

6. Comparison of the Semtner-Chervin Model with Direct Measurements

The acoustically derived barotropic large-scale currents and areal average relative vorticity can be used to check the order of magnitude and timescales of the variability of the same quantities computed from numerical general circulation model results. The Semtner-Chervin eddy resolving model [*Semtner and Chervin,* 1988] of ocean circulation gives currents at a number of depths and at half-degree intervals using primitive equations driven by a seasonal wind field. *Semtner and Chervin* [1988] compared their model output with variability observed in regions such as the Gulf Stream, Kuroshio, and Agulhas currents; here the comparison is made for the mid-Pacific ocean. Figure 9 shows the Semtner-Chervin model currents and relative vorticity projected onto the transceiver triangle in the tenth model year of wind forcing. The variability of the Semtner-Chervin results is generally smaller than that of the direct measurements (Table 3).

7. Discussion and Conclusions

Acoustically determined tidal amplitudes and phases, representing a well-known, large-scale, barotropic signal, agree with those determined from current meter data and differ slightly from the Schwiderski and CRS numerical tide models. Low-frequency barotropic currents determined acoustically show much less variability than current meter point measurements of the barotropic flow, as expected, since the acoustic measure-

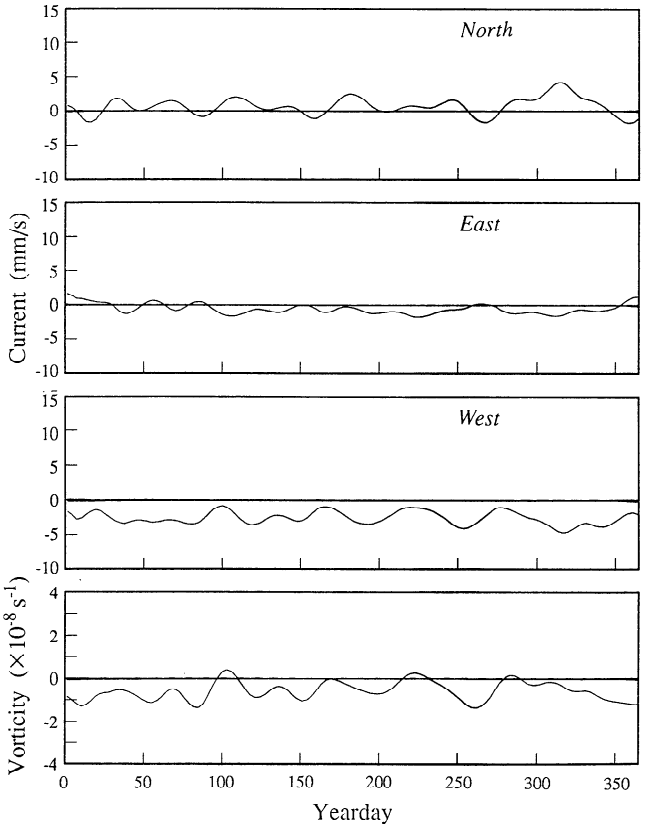

Figure 9. Currents and relative vorticity of the Semtner-Chervin model in the tenth model year. These currents have been determined by projecting the Semtner-Chervin barotropic current field onto the experiment triangle before range averaging. The vorticity is calculated by integrating the currents around the experiment triangle.

ments strongly suppress small and mesoscale variability. Areally averaged relative vorticity was also measured, but no other estimates of relative vorticity are available for comparison. Much of the variability observed in the measurements of current cancels in the calculation of vorticity, which can be expected since the dominant variability in the experiment region at periods of a few days or longer is at the megameter wavelengths [*Chave et al.*, 1992].

The conditions of this experiment are well suited to testing the validity of the Sverdrup response to wind forcing, but the observed megameter-scale variability is an order of magnitude larger than the Sverdrup response computed using the FNOC wind field. One previous experiment found some evidence for the topographic Sverdrup balance during winter, when the variance of currents increase [*Koblinsky et al.*, 1989], indicating that our conclusions might have differed had our experiment extended longer. The results of *Luther et al.* [1991] show no increase in variability in this region during the 1986–1987 winter, however. It is apparent that the Sverdrup response can be much smaller than the nonlocally forced current, which is consistent with the results of *Chave et al.* [1992]. We have verified experimentally, within the bounds of our short record length, that the time derivative of relative vorticity is unimportant to the Sverdrup balance.

The direct measurements are similar to but more energetic than the estimates of the Semtner-Chervin eddy-resolving model of ocean circulation for the variability of large-scale currents and relative vorticity in this region. This comparison provides an additional region in which the model has been tested against observations.

The experiment region is characterized by a number of temperature and/or salinity fronts [*Roden*, 1984; DWCHa]. The zonal geostrophic currents calculated by *Roden* [1984] using meridional CTD sections were about 10 cm/s and concentrated within narrow bands. Had the north leg of the experiment triangle been located within one of these narrow bands of large current, greater zonal currents and a much larger relative vorticity would have been observed.

The acoustically derived change in heat content, when compared with air-sea heat exchange, shows that advection contributes significantly to the large-scale heat budget (DWCHb). The present results for current can be combined with the hydrographically determined horizontal temperature gradient to estimate an order-of-magnitude contribution of advection to the heat budget. Since the temperature field is nearly uniform zonally, we assume that meridional advection of heat dominates. Though only the depth-averaged current has been determined, a northward surface current of 5 cm/s is not inconsistent with the observed current. The range-averaged, near-surface, meridional temperature gradient on the east leg is -0.006°C km^{-1}, which when multiplied by the assumed surface current, gives 3×10^{-7} °C s^{-1} as the average rate of near-surface temperature change on the east leg. Over a 100-day period this warming changes the heat content in the top 100 m by about 1×10^{9} J m^{-2}, which is comparable to the discrepancy between the observed heat content change and the heat input from the atmosphere. This calculation shows that the observed advection can account for the observed heat content discrepancy, though it has relied on a number of assumptions.

Appendix: Inversion of Differential Travel Times for Depth-Averaged Currents

This appendix gives a brief summary of the inverse method used to compute depth-averaged currents from the differential travel times. Equations (5) and (6) in the main body of the paper define

$$\Delta t_i = \sum_j G_{ij} A_j + \varepsilon_i$$

where $G_{ij} = -2\int_{\Gamma_i} \{[F_j(\mathbf{x})\cos\theta]/[c_0(\mathbf{x},t)^2]\}ds$, $\Delta t_i = (T_i^+ - T_i^-)$, and ε_i is data noise.

Inverse theory provides a solution for the A_j from the Δt_i [*Aki and Richards*, 1980]. In acoustic tomography this problem is most often underdetermined. One requires an a priori model covariance matrix, $(\mathbf{R_{mm}})_{jj} = <(A_j)^2>$ (assumed diagonal) and an a priori data noise covariance matrix $(\mathbf{R_{nn}})_{ii} = <(\varepsilon_i)^2>$ (also diagonal). Then, using matrix notation,

$$\mathbf{R_{dd}} = \mathbf{G}\,\mathbf{R_{mm}}\,\mathbf{G^T} + \mathbf{R_{nn}}$$

$$\mathbf{L} = \mathbf{R_{mm}}\,\mathbf{G^T}\,\mathbf{R_{dd}^{-1}}$$

The $\mathbf{L}$ is the inverse operator particular to the choice of ocean model and a priori variances. The model solution is

$$\hat{\mathbf{m}} = \mathbf{L}\,\Delta\mathbf{t}$$

where $\Delta\mathbf{t}$ is a column vector. The model error covariance matrix is

$$\mathbf{E} = \mathbf{R_{mm}} - \mathbf{L}\,\mathbf{G}\,\mathbf{R_{mm}}$$

$\mathbf{L}\,\mathbf{G}$ is the resolution matrix: $\hat{\mathbf{m}} = \mathbf{L}\,\mathbf{G}\,\mathbf{m}$, where $\mathbf{m}$ is the "true" solution for the A_j.

The inverse solution for the model amplitudes can be transformed to a range and depth average by an "integral" operator $\mathbf{W}$.

$$\bar{U} = \mathbf{W^T}\,\hat{\mathbf{m}}$$

$$\bar{E} = \mathbf{W^T}\,\mathbf{E}\,\mathbf{W}$$

Here $\bar{U}$ and $\bar{E}$ are the depth-averaged current and uncertainty variance, respectively. In the calculation of $\bar{E}$, the depth-correlated error is taken into account.

The major difficulty with the solution $\hat{\mathbf{m}}$ is that it is often sensitive to the choice of ocean model and assumed a priori variances. Because of the depth-integrating nature of the ray paths, $\bar{U}$ is well defined, though $\hat{\mathbf{m}}$ may not be.

The above formalism is also used to estimate the tidal harmonic constants and their uncertainty from the time series of depth-averaged current. The barotropic tidal current is represented as

$$U(t_i) = \sum_{N=1}^{8} a_N \cos(\omega_N t_i - \phi_N) + \varepsilon_i$$

where the ω_N are the frequencies of the major tidal constituents (K_2, S_2, M_2, N_2, K_1, P_1, O_1, and Q_1), a_N and ϕ_N are the amplitude and phase, respectively, and ε_i is noise. More conveniently,

$$U(t_i) = \sum_{N=1}^{8} b_N \cos(\omega_N t_i) + \sum_{N=1}^{8} c_N \sin(\omega_N t_i) + \varepsilon_i$$

with

$$a_N = \sqrt{b_N^2 + c_N^2}, \quad \phi_N = \mathrm{atan}\left(\frac{c_N}{b_N}\right)$$

To determine the tidal harmonic constants, the data are the time series of barotropic current. In the inverse formalism,

$$G_{ij} = \cos(\omega_j t_i) \text{ or } \sin(\omega_j t_i)$$

and once the A_j (which are the set { b_N, c_N }) and their uncertainties are found, the harmonic constants and their uncertainties can be found from them. The noise term is the combination of the uncertainty in the barotropic current estimates from the travel times and, predominantly, nontidal current variance. Unweighted least squares are first employed to give initial estimates of the b_N and c_N and the nontidal variance. With these initial estimates, the inverse is then used to finally estimate the b_N and c_N, together with the uncertainties. The tidal harmonic constants do not significantly depend on their initial estimates or the assumed noise.

Acknowledgments. R. Spindel played a key role in the early design of the experiment. Credit for the success of the experiment belongs largely to the dedicated personnel who designed, fabricated, tested, and fielded the equipment: S. Abbott, K. Hardy, D. Horwitt, J. Kemp, S. Liberatore, D. Peckham, and R. Truesdale. B. Ma helped with the programming. We are grateful to D. Luther for providing us with valuable discussion and the data allowing the comparison of the acoustically derived currents with the current meter and electromagnetic measurements. We also thank D. Luther for urging us to take into account the topographic effects in the Sverdrup balance and for suppling the FNOC data. E. Schwiderski and D. Cartwright provided their model estimates of the tidal currents. C. S. Chiu supplied the Semtner-Chervin model results. This work was supported by National Science Foundation grants OCE-82-14918 and OCE-84-14978 and Office of Naval Research contracts N00014-80-C-0217, N00014-84-G-0214, N00014-87-K-0120, and N0014-87-K-0760.

References

Aki, K., and P. G. Richards, *Quantitative Seismology, vol. 2*, 373 pp., Freeman, Cooper, San Francisco, Calif., 1980.

Brink, K.H., Evidence for wind-driven current fluctuations in the western North Atlantic, *J. Geophys. Res., 94,* 2029–2044, 1989.

Cartwright, D.E., R.D. Ray, and B.V. Sanchez, A computer program for predicting oceanic tidal currents, *NASA Tech. Memo. 104578,* 21 pp., 1992.

Chave, A.D., D.S. Luther, and F.H. Filloux, Gyre-scale current measurements using reciprocal acoustic transmissions, *Proc. IEEE Work. Conf. Current Meas., 4,* 65–70, 1990.

Chave, A.D., D.S. Luther, and J.H. Filloux, Variability of the wind stress curl over the North Pacific: Implications for the oceanic response, *J. Geophys. Res., 96,* 18,361–18,379, 1991.

Chave, A.D., D.S. Luther, and J.H. Filloux, The barotropic electromagnetic and pressure experiment, 1, Barotropic current response to atmospheric forcing, *J. Geophys. Res., 97,* 9565–9593, 1992.

Cummins, P.F., The barotropic response of the subpolar North Pacific to stochastic wind forcing, *J. Geophys. Res., 96,* 8869–8880, 1991.

Dushaw, B.D., P.F. Worcester, B.D. Cornuelle, and B.M. Howe, On equations for the speed of sound in seawater, *J. Acoust. Soc. Am., 93,* 255–275, 1993a.

Dushaw, B.D., P.F. Worcester, B.D. Cornuelle, and B.M. Howe, Variability of heat content in the central North Pacific in summer 1987 determined from long-range acoustic transmissions, *J. Phys. Oceanogr., 23,* 2650–2666, 1993b.

Emery, W.J., On the geographical variability of the upper level mean and eddy fields in the North Atlantic and North Pacific, *J. Phys. Oceanogr., 13,* 269–291, 1983.

Flatté, S.M., R. Dashen, W. Munk, K.M. Watson, and R. Zachariasen, *Sound Transmission Through a Fluctuating Ocean*, Cambridge University Press, New York, 1979.

Howe, B.M., P.F. Worcester, and R.C. Spindel, Ocean acoustic tomography: Mesoscale velocity, *J. Geophys. Res., 92,* 3785–3805, 1987.

Koblinsky, C.J., The global distribution of f/H and the barotropic response of the ocean, *J. Geophys. Res., 95,* 3213–3218, 1990.

Koblinsky, C.J., P.P. Niiler, and W.J. Schmitz, Jr., Observations of wind-forced deep-ocean currents in the North Pacific, *J. Geophys. Res., 94,* 10,773–10,790, 1989.

Large, W.G., and S. Pond, Open ocean momentum flux measurements in moderate to strong winds, *J. Phys. Oceanogr., 11,* 324–336, 1981.

Longuet-Higgins, M., On triangular tomography, *Dyn. Atmos. Oceans, 7,* 33–46, 1982.

Luther, D.S., A.D. Chave, and J.H. Filloux, BEMPEX: A study of barotropic ocean currents and lithospheric conductivity, *Eos Trans. AGU, 68,* 618–619, 628–629, 1987.

Luther, D.S., A.D. Chave, J.H. Filloux, and P.F. Spain, Evidence for local and nonlocal barotropic responses to atmospheric forcing during BEMPEX, *Geophys. Res. Lett., 17,* 949–952, 1990.

Luther, D.S., J.H. Filloux, and A.D. Chave, Low-frequency motionally induced electromagnetic fields in the ocean, 2, Electric field and Eulerian current comparison, *J. Geophys. Res., 96,* 12,797–12,814, 1991.

Müller P., and C. Frankignoul, Direct atmospheric forcing of geostrophic eddies, *J. Phys. Oceanogr., 11,* 287–308, 1981.

Munk, W.M., and D.E. Cartwright, Tidal spectroscopy and prediction, *Philos. Trans. R. Soc. London, Ser. A, 259,* 533–581, 1966.

Munk, W., and C. Wunsch, Observing the ocean in the 1990's, *Philos. Trans. R. Soc. London, Ser. A, 307,* 439–464, 1982.

Munk, W., B. Zetler, J. Clark, S. Gill, D. Porter, J. Spiesberger, and R. Spindel, Tidal effects on long-range sound transmission, *J. Geophys. Res., 86,* 6399–6410, 1981.

Niiler, P.P., and C.J. Koblinsky, A local, time-dependent Sverdrup balance in the eastern North Pacific Ocean, *Science, 229,* 754–756, 1985.

Pazan, S.E., T.P. Barnett, A.M. Tubbs, and D. Halpern, Comparison of observed and model wind velocities, *J. Appl. Meteorol., 21,* 314–320, 1982.

Roden, G.I., Mesoscale oceanic fronts of the North Pacific, *Ann. Geophys., 2,* 399–410, 1984.

Rossby, T., An oceanic vorticity meter, *J. Mar. Res., 33,* 213–222, 1975.

Samelson, R.M., Evidence for wind-driven current fluctuations in the eastern North Atlantic, *J. Geophys. Res., 95,* 11,359–11,368, 1990.

Schureman, P., Manual of harmonic analysis and prediction of tides, *Spec. Publ. 98,* 317 pp., U.S. Coast and Geod. Surv., U.S. Govt. Print. Off., Washington, D.C., 1958.

Schwiderski, E.W., Ocean tides, I, Global tide equations, II, A hydrodynamical interpolation model, *Mar. Geod., 3,* 161–255, 1980.

Schwiderski, E.W., Global ocean tides, X, The fortnightly lunar tide (Mf) atlas of tidal charts and maps, *TR 82-151,* Nav. Surface Weapons Cen., Dahlgren, VA., February 1982.

Semtner, A.J., and R.M. Chervin, A simulation of the general ocean circulation with resolved eddies, *J. Geophys. Res., 93,* 15,502–15,522, 1988.

Shum, C.K., R.A. Werner, D.T. Sandwell, B.H. Zhang, R.S. Nerem, and B.D. Tapley, Variations of global mesoscale eddy energy observed from Geosat, *J. Geophys. Res., 95,* 17,865–17,876, 1990.

Sverdrup, H.U., Wind-driven currents in a baroclinic ocean; With application to the equatorial currents of the Eastern Pacific, *Proc. Natl. Acad. Sci., 33,* 318–326, 1947.

Willebrand, J.S., G.H. Philander, and R.C. Pacanowski, The oceanic response to large-scale atmospheric disturbances, *J. Phys. Oceanogr., 10,* 411–429, 1980.

Worcester, P.F., R.C. Spindel, and B.M. Howe, Reciprocal acoustic transmissions: Instrumentation for mesoscale monitoring of ocean currents, *J. Oceanic Eng., OE-10,* 123–137, 1985.

Worcester, P.F., B. Dushaw, and B.M. Howe, Gyre-scale current measurements using reciprocal acoustic transmissions, *Proc. IEEE Work. Conf. Current Meas., 4,* 65–70, 1990.

Worcester, P.F., B. Dushaw, and B.M. Howe, Gyre-scale reciprocal acoustic transmissions, in *Ocean Variability and Acoustic Propagation*, edited by J. Potter and A. Warn-Varnas, pp. 119–134, Kluwer Academic, Norwell, Mass., 1991.

B.D. Cornuelle and P.F. Worcester, Scripps Institution of Oceanography, La Jolla, CA 92093-0230.

B.D. Dushaw, Applied Physics Laboratory, College of Ocean and Fishery Sciences, University of Washington, 1013 N.E. 40th Street, Seattle, WA 98105-6698.

B.M. Howe, Applied Physics Laboratory, College of Ocean and Fishery Sciences, University of Washington, Seattle, WA 98105-6698.

(Received May 7, 1993; revised September 9, 1993;
accepted October 15, 1993.)